Remote Sensing of Environment 225 (2019) 93–106

Contents lists available at ScienceDirect

Remote Sensing of Environment

journal homepage: www.elsevier.com/locate/rse

Roughness and vegetation change detection: A pre-processing for soil moisture retrieval from multi-temporal SAR imagery

Liujun Zhu*, Jeffrey P. Walker, Nan Ye, Christoph Rüdiger

Department of Civil Engineering, Monash University, Clayton, Vic. 3800, Australia

ARTICLE INFO

Keywords:
Soil moisture
Surface roughness
Vegetation
Time series analysis
Change detection

ABSTRACT

Multi-temporal analysis has been widely acknowledged as a promising method to derive soil moisture from radar backscatter observations. The method assumes that only soil moisture varies in the period of interest, while all other parameters such as vegetation water content and soil surface roughness are sufficiently time invariant. However, this assumption is not easy to satisfy in agricultural areas where cultivation practices such as ploughing and irrigation are irregularly conducted between radar acquisitions. The paper has proposed an unsupervised change detection method to serve as a pre-processing procedure for multi-temporal retrieval. Briefly, the temporal ratio of HV and the temporal difference of HV/VV and VV polarizations were selected as the optimal feature space, using a genetic algorithm based feature selection algorithm and an extensive synthetic data set. The change map is determined from a two-step procedure with the first step producing multiple over-detected change maps for the period of interest using the Density-Based Spatial Clustering of Applications with Noise (DBSCAN) method. The second step merges the multiple change maps to remove the false alarms with a principle similar to the ensemble machine learning. Evaluation on a synthetic data set demonstrated that the proposed method can largely remove the error in multi-temporal soil moisture retrieval that is caused by abrupt roughness and vegetation changes. Evaluation on real radar data sets, including airborne L-band radar, RADARSAT-2 at C-band and COSMO SkyMed at X-band, demonstrated an accurate identification (>0.9) while yielding a low false-alarm rate (<0.1). These results suggest that the method may be used as a pre-processing stage of global soil moisture retrieval from radar satellite missions with a high revisit frequency, such as Sentinel-1 and SAOCOM-1.

1. Introduction

Synthetic Aperture Radar (SAR) has been demonstrated as a promising way to retrieve surface soil moisture from satellite at a spatial resolution of better than 100 m, due to its all-weather capability and the high sensitivity of backscatter to surface soil moisture (Ulaby et al., 2014). However, soil moisture retrieval from SAR data still faces some key problems, with the main challenge being the large number of surface parameters affecting the radar backscatter (in particular surface roughness and vegetation structure).

A great number of soil moisture retrieval algorithms have been proposed over the last four decades, across three main categories, i.e. empirical methods, inversion of scattering models and multi-temporal analysis (Kornelsen and Coulibaly, 2013). Among these, multi-temporal analysis has been acknowledged as the most promising method, because of its simplicity in decoupling the effect of soil moisture on radar backscatter from that of other surface parameters (Balenzano et al., 2011). Soil roughness and vegetation parameters undergo relatively smooth evolution in time compared to soil moisture, with the exception being the area with cultivation practices, and thus can be assumed constant for acquisitions with a sufficiently short time interval. The utilization of this assumption in soil moisture retrieval starts from Wagner et al. (1999a, 1999b), which relates the backscatter of each pixel to that of wettest and driest soil moisture conditions using image ratios or differences of backscatter observations at different times. Recently, several algorithms that invert temporal backscatter difference/ratio for soil moisture retrievals have been proposed for operational soil moisture mapping using Sentinel-1 and/or Soil Moisture Active and Passive (SMAP) time series (Balenzano et al., 2011; Balenzano et al., 2013; Ouellette et al., 2017).

Multi-temporal SAR data can also circumvent the problem of ill-posed inversion of scattering models by introducing more observations. A number of studies have directly estimated time-series soil moisture, together with a constant root mean square (RMS) height (s) and/or

* Corresponding author.
E-mail address: Liujun.Zhu@monash.edu (L. Zhu).

https://doi.org/10.1016/j.rse.2019.02.027
Received 24 January 2019; Accepted 28 February 2019
Available online 06 March 2019
0034-4257/

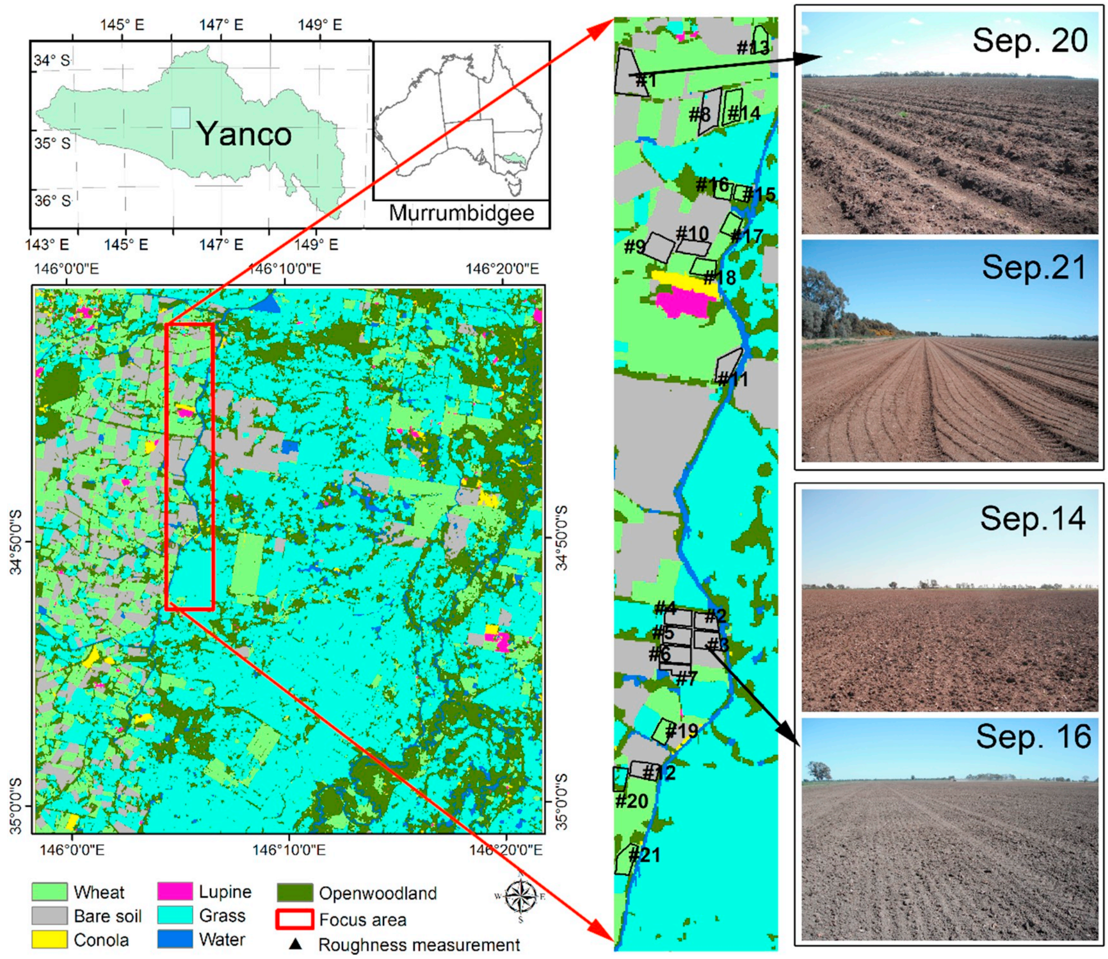

Fig. 1. Focus area selected for algorithm evaluation using ground measurements with the changed paddocks outlined and numbered. The right panel shows two examples where roughness changed during the period of SMAPEx-5.

correlation length (l), through inversion of scattering models from time-series backscatter measurements (Kim et al., 2012; Kweon and Oh, 2014; Mattia et al., 2009; Notarnicola, 2014; Pierdicca et al., 2010). Others have combined multi-angular time-series data to first determine surface roughness parameters and then retrieved soil moisture from the successive observations (Rahman et al., 2008; Sahebi and Angles, 2010; van der Velde et al., 2012; Wang et al., 2011).

Despite the great potential of using multi-temporal SAR imagery, the assumption that the variation of backscatter in time only relates to changes of soil moisture may not be valid, even for two successive images from the Sentinel-1 constellation (6 days). A heavy rainfall between two observations can cause impulse smoothening of the soil roughness (Zobeck and Onstad, 1987) and significant change of the vegetation's dielectric constant (McDonald et al., 2002). Fortunately, the presence/absence of a rainfall event is relatively easy to be determined, because a rainfall event can result in an abrupt increase of average backscatter over time. However, backscatter variations can also occur at the paddock scale due to cultivation activities, e.g. irrigation, harvesting, ploughing and harrowing. One soil moisture retrieval approach that considers the paddock scale roughness changes includes the Bayesian change detection method (Notarnicola, 2014). A more favorable approach is to include a pre-processing procedure that can determine the changed paddocks, making detection independent of the aforementioned multi-temporal approaches. With knowledge of changed paddocks, time series SAR data of change paddocks can then be split into different subseries according to the paddock specific changed dates, where multi-temporal retrieval methods can be used safely.

A great number of methods have been proposed for detecting earth surface changes using multi-temporal SAR data, with the main interest focusing on change of landcover types (e.g., Marin et al., 2015; Pantze et al., 2014), flooded area (e.g., Brisco et al., 2013), ship movements (e.g., Wei et al., 2014) and oil spills (e.g., Konik and Bradtke, 2016). There are two main steps in change detection (Bruzzone and Prieto, 2002): one is the generation and selection of features (e.g. the difference/ratio maps) at a pixel and/or object basis; the other analyzes the differences between images and identifies the changes. The former is tightly related to specific changes because of their different scattering mechanisms. For the latter, popular methods include an automatic Bayesian algorithm (Bruzzone and Prieto, 2002), a Kittler-Illingworth based method (Satalino et al., 2014), and a method based on enhanced fuzzy clustering (Gong et al., 2012). Despite the promising performance of these methods in specific applications, two issues need to be further addressed: i) Can slight changes in roughness and vegetation be identified? and ii) What are the optimal polarizations and spatial scale combination in identifying these changes?

The study has developed an anomaly detection method as a pre-processing step for the safe use of multi-temporal approaches. The spatial/temporal characteristics of roughness and vegetation changes in SAR data were first investigated to guide the development of the method. The proposed method includes two main components: i) extraction of the optimal image ratio/difference for change detection at the paddock scale with the aid of a feature selection algorithm, and ii) a two-step algorithm to identify the changed paddocks, with the first step generating multiple over-detection for the same period of interest using different SAR image pairs, which are then combined to remove the false alarms in the second step. The proposed pre-processing method was evaluated using extensive synthetic and real SAR data sets. The multi-temporal soil moisture retrieval method proposed by Wagner et al. (1999a, 1999b) was then used to show the initial and residual errors caused by abrupt roughness and vegetation changes before and after application of the proposed method.

2. SMAPEx-5 dataset

2.1. Ground measurements

The Fifth Soil Moisture Active Passive Experiment (SMAPEx-5) was an airborne field campaign that contributed to the calibration and validation of NASA's Soil Moisture Active Passive (SMAP) mission (Ye et al., submitted). This campaign was carried out in the Australian Spring (7th–27th September 2015) in the Yanco agricultural area of south-eastern Australia, with the focus area selected for this study shown in Fig. 1. The main land cover types for the focus area included dense winter wheat, grass and bare soil, with part of the area undergoing intensive cultivation practices during the later stage of the SMAPEx-5 period. All paddocks with cultivation activities in the focus area were recorded for ground truth, including 8 irrigated wheat paddocks and 13 bare soil or grass paddocks. These paddocks account for a small part of the focus area, with their boundary and paddock ID depicted in Fig. 1.

Extensive ground sampling of near-surface (0–5 cm) soil moisture (*mv*) was carried out on eight days during SMAPEx-5 (September 9th, 11th, 14th, 17th, 19th, 22nd, 24th and 27th). Measurements were made using portable soil moisture sensors on a regular grid with a spacing of 250 m. Three point-based soil moisture measurements were made within a 1 m radius at each sampling location and averaged to account for small-scale soil moisture variability. A moderate rainfall of ~18 mm occurred before the experiment resulting in high *mv* values of ~0.40 m^3/m^3 at the start followed by a three-week dry down period. The gradually changing rate can be roughly expressed as $1 - e^{(-I/2)}$ with the I being the order of sampling dates from 1 to 8 according to the ground sampling data (Ye et al., submitted).

Roughness was measured along 3 m segments using a pin profiler with pins at 0.5 cm spacing. Measurements were made in two orthogonal directions (along and across rows or north-south and east-west in the case of no row structure), and at two to three locations within each paddock, to characterize spatial variability in surface roughness. In general, the root mean square height (s) and correlation length (cl) ranged from 0.5 to 3 cm and 5 to 35 cm for isotropic surface respectively. However, s values in paddocks with row structures up to 9 cm were observed across the row.

Intensive vegetation sampling, including plant height, stem and leaf geometry, and vegetation water content (VWC), was carried out between the soil moisture sampling days. The available measurements for paddocks with cultivation activities during the experiment are listed in Table 1. Unfortunately, most of the cultivation events occurred between the last two soil moisture sampling dates (DOY 267 and 269). Consequently, the occurrence of these events was recorded on the last soil moisture sampling date (DOY 269) without any detailed measurements of the roughness and vegetation changes.

2.2. SAR data set

Time series of SAR data at three different microwave frequencies, i.e., L-band (1.26 GHz), C-band (5.4 GHz) and X-band (9.3 GHz), were used in this study. A summary (acquisition dates, pass direction, frequency and polarization) of these data sets is provided in Fig. 2. The L-band data set was acquired during SMAPEx-5 using the airborne Polarimetric L-band Imaging SAR (PLIS) with incidence angles ranging from 15° to 50° across an ~2 km swath. The spacing of PLIS single look complex (SLC) data is 2 m in azimuth and 3.75 m in slant range (for details of the PLIS system and its calibration refer to Zhu et al., 2018b). Three RADARSAT-2 wide-swath standard quad-polarization SLC products and four standard dual polarization SLC products were available during SMAPEx-5 with a slant range spacing of 8 or 11.8 m and an azimuth spacing of 5.1 m. The incidence angle of these images varied between 22° and 40°. The X-band data set consists of two interferometric subsets of the COSMO-SkyMed STRIPMAP HIMAGE acquired from left and right look directions, respectively. The ground range and azimuth spacing of these images is 3 m. An optical image acquired by Landsat 8 Operational Land Imager (OLI) on 30th September 2015 was used as a reference for geo-registration.

Images from all three sensors were multi-looked and re-sampled to a grid size of 25 m. The cosine law (Ulaby et al., 1982) with a power index of 2 was used to normalize the backscattering coefficient (dB) to a reference angle of 30°. Since this can have a negative effect on change detection, the proposed method could be applied to data with similar incidence angle ranges in turn, with the presence/absence of roughness and vegetation changes being combined using logical operations. Alternatively, as a pre-processing stage of multi-temporal soil moisture retrieval, the one used in a specific retrieval study/application could also be the optimal choice.

2.3. Cultivation activities in SAR data

The PLIS time series data over the focus area (the red rectangle in Fig. 1) and the records of cultivation practices between DOY 267 and 270 in 2015 were used to provide an opportunity to investigate the spatial and temporal characteristics of anomaly surface changes. Fig. 3(b), (c) and (d) shows the difference maps of HH, VH and VV polarized backscatter images acquired on DOY 267 and 270. Ploughing and irrigation practices were observed over five bare soil paddocks and eight winter wheat fields in this period, respectively, with these cultivation practices being carried out for individual paddocks. Quite different patches are apparent in the difference maps with the boundaries of these patches roughly matching that of these paddocks. Accordingly, it is reasonable to treat all pixels describing a single paddock as an object and applying object-based techniques to detect the changed paddocks. Object-based techniques take the irregular geographical objects in the research area (i.e. the paddocks in this study) as the analysis unit rather than the uniform pixel/grid, with the first step being image segmentation to determine the boundaries of geographical objects. For SMAPEx-5 (Yanco area), the area of paddocks ranged from 0.1 km^2 to 0.5 km^2, making this the target scale of the study. However, soil moisture retrieval can still be carried out at a finer scale by simply taking the detection results as a spatial mask. The use of an object-based analysis helps to reduce the effect of geo-referencing and speckle noise (Hussain et al., 2013), thus reducing the uncertainty caused by data pre-processing.

The time series HH, VH and VV of four bare soil paddocks with soil practices (i.e., #9–12) and four wheat paddocks with irrigation (i.e., #16–19) are also depicted in Fig. 3. Others were not included for simplicity and because of their similar behavior. In general, the backscattering coefficients for all polarizations gradually decreased over the whole period of DOY 252–270, which is coincident with the decrease of soil moisture over the SMAPEx-5. A significant increase of HH, VH and VV can be observed from DOY 267 to 270 over the winter wheat paddocks due to irrigation. Similar results were found across bare soil paddocks due to soil cultivation activities. However, these changes were generated by different mechanisms. The relationship between irrigation and surface changes is quite complex. Despite a significant increase of soil moisture, irrigation can decrease soil roughness over a short time (Hunsaker et al., 1999). The sudden increase of soil water can also change the dielectric constant of wheat, with a similar magnitude effect to that of rainfall (McDonald et al., 2002). With respect to soil cultivation, the soil moisture of the top layer and roughness can be changed simultaneously. As a result, it can be hard to determine the

Table 1
Roughness and vegetation measurements of the paddocks with cultivation activities.

Paddock #	Landcover	VWC (kg/m^2)	Row azimuth	Before cultivation		After cultivation		Cultivation activity DOY
				*s** (cm)	*cl/s**	*s** (cm)	*cl/s**	
1	Bare	–	90	1.94(8.66)	6.82(2.44)	0.51(5.47)	5.32(20.7)	264
2–3	Bare	–	–	–	–	–	–	258
4–7	Bare	–	–	–	–	–	–	263
8	Bare	–	10	–	–	1.16(5.54)	8.24(3.65)	263
9	Bare	–	–	1.50	14.65	1.90	6.05	268
10	Bare	–	90	2.12(6.30)	7.76(3.20)	–	–	269
11	Bare	–	–	–	–	–	–	268
12	Bare	–	–	–	–	–	–	268
13	Wheat	–	–	–	–	–	–	269
14	Wheat	3.72	10	1.01(2.94)	11.30(6.49)	–	–	269
15	Wheat	2.81	90	1.06(2.76)	7.24(4.98)	–	–	269
16	Wheat	1.17	–	–	–	–	–	269
17	Wheat	2.32	–	–	–	–	–	269
18	Wheat	2.82	90	1.54(2.83)	6.95(5.34)	–	–	269
19, 20	Wheat	–	–	–	–	–	–	269
21	Wheat	2.78	–	1.60	7.44	–	–	269

–: not available.
* Roughness along (perpendicular) to row structure for paddocks with periodic surface.

contribution of soil moisture change to the measured backscatter variation. Nevertheless, for detecting these anomalies, it is not critical what causes the backscatter variation. Since the changed paddocks commonly takes only a small part of the whole research area, and the SAR observations of these paddocks deviate a lot in both space and time from that of other paddocks, the changed paddocks may be treated as outliers.

Fig. 3 also illustrates the sensitivity of different polarizations to these changes. The increase in VH backscatter for all bare soil paddocks was somewhat higher than that in HH and VV from DOY 267 to 270, which can be explained by the different polarization sensitivities to soil roughness. Irrigated paddocks showed significant backscatter increase in all three polarizations. A feature space (e.g. the 2-dimension space spanned by temporal difference of HV and VV) with larger sensitivity is commonly more powerful in detecting the changed paddocks than one with smaller sensitivity. For multi-temporal polarimetric data, thousands of feature spaces are available and thus a feature selection algorithm is needed to find the optimal feature space.

3. Synthetic data set

The cultivation practices observed during SMAPEx-5 cannot fully represent all possible anomaly changes in real applications. Accordingly, a synthetic SAR data set was generated with various soil moisture, roughness and vegetation changes based on the SMAPEx-5 ground measurements for a comprehensive evaluation. The landcover of the SMAPEx-5 focus area was selected as the base map for the synthetic study with a total of 621 paddocks. In this section, the detail of synthetic roughness, vegetation and soil moisture was introduced first, followed by the method to build synthetic radar data and the evaluation process over the generated synthetic data set.

3.1. Synthetic surface parameters

Eight soil moisture maps were generated with a time step of 2–3 days according to the eight sampling dates of SMAPEx-5. Specifically, the day 1 average soil moisture value (m^3/m^3) of each paddock was randomly generated from a uniform distribution of U (0.25, 0.4). From this paddock average value, the soil moisture of each pixel of the paddock was randomly generated from a normal distribution with a standard deviation of 0.05 (m^3/m^3) to account for intra paddock variability. The dry down process observed during SMAPEx-5 (described in Section 2.1) was subsequently used to produce the following seven soil moisture maps.

After soil cultivation activities, both the observed *s* and *cl* changed (Table 1). However, the changes of *s* and *cl* can be hardly independent in real applications. Different empirical relationships between *s* and effective *cl* have been observed for various radar configurations in forward prediction, e.g., Baghdadi et al. (2004); Baghdadi et al. (2002), with a fixed *cl/s* ratio of 10 suggested by Kim et al. (2012) for soil moisture mapping at 3-km resolution for L-band data. Moreover, additional parameters are required for soil surfaces with a periodical row structure, as the effect of row structure and their temporal change on backscatter is quite complex to model (Blaes and Defourny, 2008; Zribi et al., 2002). Fortunately, this study only needed to determine the presence/absence of roughness changes, meaning that it was unnecessary to know the specific kind of change. As different types of roughness changes, including the correlation function shape, row structure, *s* and *cl*, can all result in similar changes in radar observations, equivalent changes of *s* can always be found for all potential roughness changes. Accordingly, only *s* was simulated independently with the exponential correlation function and a fixed *cl* of 10*s*. The *s* was chose as the dependent variable due to its significantly higher

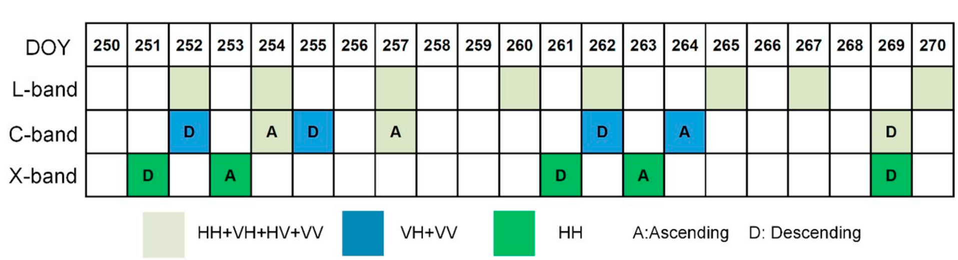

Fig. 2. Summary of PLIS (L-band), RADARSAT-2 (C-band) and COSMO SkyMed (X-band) data used in this study, showing acquisition date (day of year), frequency, polarization and orbit.

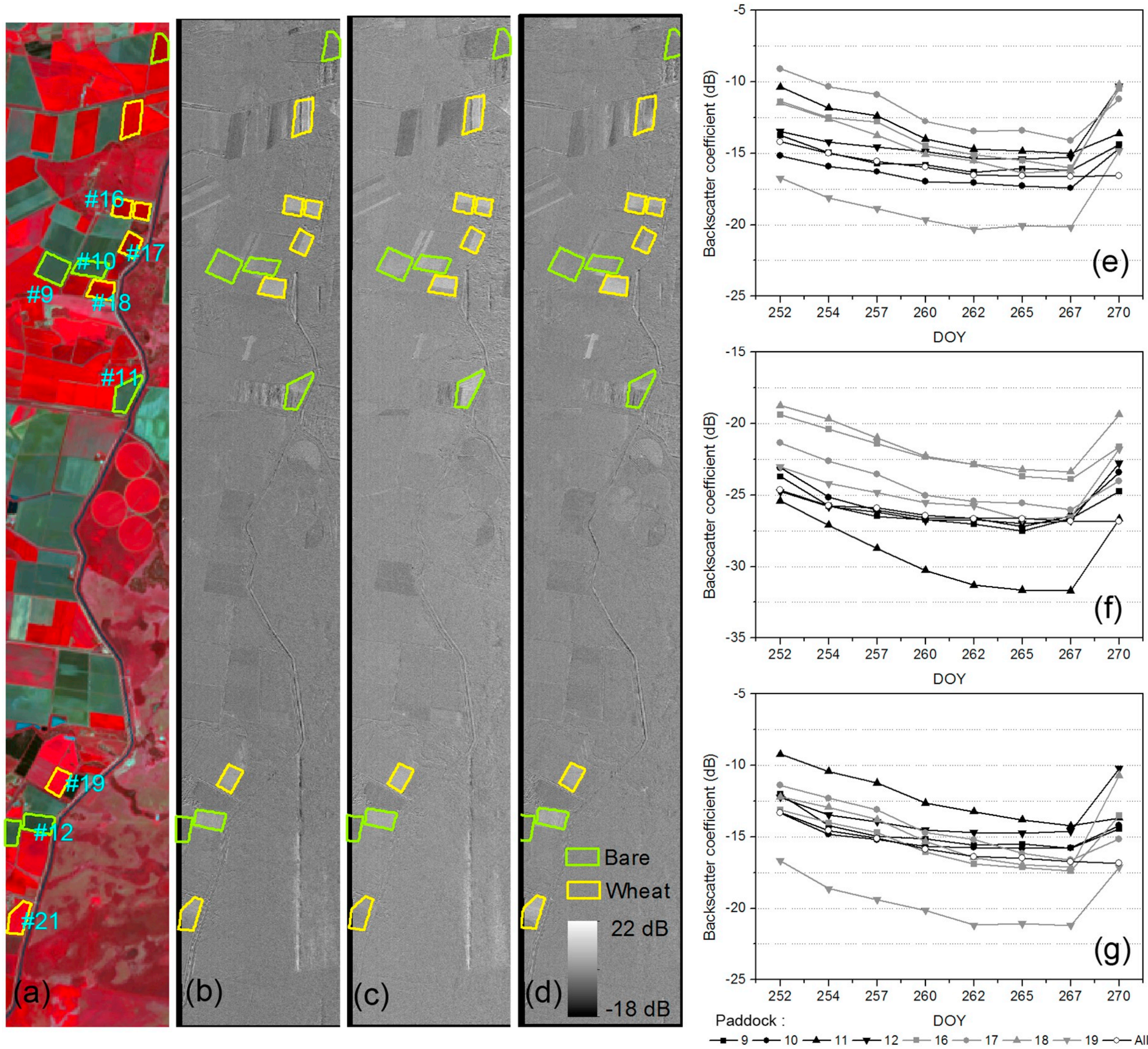

Fig. 3. Anomaly surface changes at L-band (PLIS) multi-temporal SAR images. Panel (a) shows the changed paddocks observed between DOY 267 and 270, 2015 on a false color composite Landsat 8 OLI image (RGB: near-infrared/red/green); panels (b), (c), and (d) are the backscatter difference maps in HH, HV and VV polarizations respectively between images acquired on DOY 267 and 270, with the changed paddocks also delineated, panels (e), (f) and (g) are respectively the time series HH, HV and VV of several examples, which also include the average backscattering coefficient of the whole area labeled as "All". (For interpretation of the references to color in this figure legend, the reader is referred to the web version of this article.)

sensitivity on the radar backscatter (Ulaby et al., 2014). Similar to the generation of soil moisture maps, the initial day 1 average *s* value (cm) of each paddock was randomly generated from U(0.5, 4). Individual *s* values within each paddock were then produced by randomly perturbing with a value selected from a normal distribution with a standard deviation of 0.3 cm. The gradual decreasing roughness over time was approximated by multiplying through by a factor 0.98 on each day to produce the second to eighth *s* maps.

As aforementioned, cultivation activities (e.g., harvest and irrigation) over vegetated areas can introduce changes in both the vegetation structure and biophysical parameters. In this study, a single parameter (VWC) was selected to represent the vegetation layer considering the complexity to include other parameters, with the two main vegetation types of SMAPEx-5 (wheat and grass) were considered. For the purpose of forward modeling, the vegetation layer was assumed as a random layer of lossy cylinders with a dominant vertical structure. Other vegetation parameters were determined by their allometric relationships with VWC and SMAPEx-5 ground measurements (Zhu et al., 2018a). The initial average VWC value of each paddock was randomly generated from U (0.2, 4), with individual values within each paddock being produced by imposing random perturbation according to a normal distribution with a standard deviation of 0.5 kg/m^2. Moreover, the second to eighth VWC maps were generated by multiplying the previous VWC map by 1.05 to represent crop growth.

To simulate cultivation practices, random changes were introduced into the *s* and VWC maps using a fixed probability of 10% for two successive roughness and VWC maps in time. Once a paddock was selected as having *s* or VWC changes, the average value of the paddock was randomly determined and the value of each pixel in the paddock re-generated according to the process outlined above. The input for generating these maps is summarized in Table 2. It is worth noting that the VWC of bare soil paddocks was set to 0 without allowing for changes in time.

3.2. Construction of synthetic radar data

Based on the surface parameter maps, speckle-free backscattering coefficient maps were produced using forward scattering models. For L-band, the look-up table based on Numerical Maxwell Model of Three-Dimensional simulation (NMM3D) (Huang and Tsang, 2012) was used to predict the backscattering. The Distort Born Approximation (DBA; Lang and Sighu, 1983) together with NMM3D was used for vegetated

Table 2
The input for generating time series maps of surface parameters. U (A, B) denotes a uniform distribution ranging from A to B.

Parameter	Soil moisture (m^3/m^3)	RMS height (cm)	VWC (kg/m^2)
Distribution for initial mean value	U (0.25, 0.4)	U (0.5, 4)	U (0.2, 4)
Intra-paddock standard deviation	0.5	0.3	0.5
Gradually changing rate	$1 - e^{(-I/2)}$*	0.98	1.05
Probability of anomaly change	0	10%	10% or 0
Anomaly change amplitude (%)	0	U (10, 70)	U (10, 70)

* Coincident with SMAPEx-5, I is the map time index starting from 1.

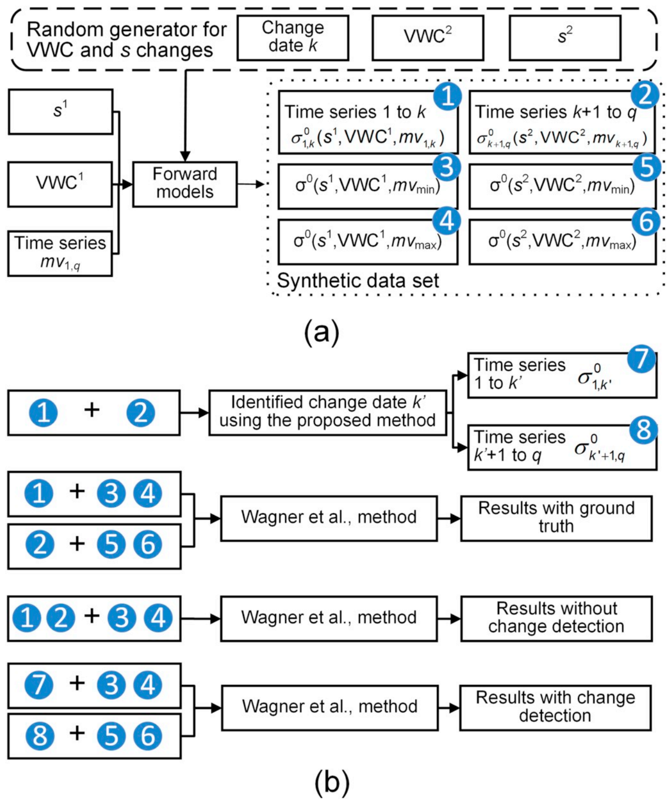

Fig. 4. Flowchart of synthetic radar data construction (a) and the validation process over the synthetic radar data using Wagner's method (b). The s and VWC are roughness RMS height and vegetation water content respectively, with the superscript 1 and 2 being the initial and changed states. $mv_{1,q}$ denotes time series soil moisture from the first to qth dates.

areas. For C-band, the Oh model (Oh, 2004) and Oh + DBA model were used for bare and vegetated areas. Only the bare soil (using the Oh model) was included in the X-band data set because it is questionable to use X-band for soil moisture retrieval under vegetation. Speckle noise maps were produced using the chi-square distribution with 2N degrees of freedom, where N is the number of independent looks (Bolter et al., 1996). The speckle-free backscattering coefficient maps were then multiplied pixel-wise with the generated speckle noise.

Fig. 4(a) shows the process of generating the time series σ^0 in dB of a given period 1 to q. For one grid with s or VWC changes at date k, two sub-series σ^0 were simulated taking the initial (s^1 and VWC^1) and changed (s^2 and VWC^2) surface parameters as the input respectively. The σ^0 of wettest ($mv = 0.43\,m^3/m^3$) and driest ($mv = 0.03\,m^3/m^3$) conditions with the initial s and VWC also generated, while an additional set of σ^0 representing wettest and driest conditions were calculated for these with s or VWC changes (parts 5 and 6 in Fig. 4a).

3.3. Validation metrics

The records of simulated anomalies and cultivation practices observed during SAMPEx-5 (Fig. 1) were used to produce reference maps for validation of synthetic and real data results, respectively. There are four possible outcomes in identifying a paddock as changed or not, when comparing the detection results and the reference maps: true positive (TP), true negative (TN), false positive (FP) and false negative (FN). Based on these, accuracy rate (AR), false alarm rate (FAR), and F score (Olson and Delen, 2008) were calculated:

$$AR = \frac{TP}{TP + FP}, \tag{1}$$

$$FAR = \frac{FN}{TP + FN}, \tag{2}$$

$$F = \frac{2TP}{2TP + FP + FN}, \tag{3}$$

The AR (also known as *precision*) and FAR reflect the missed alarms and the false alarms of change detection results, respectively, while the F score is a joint measure that penalizes both missed alarms and false alarms. For soil moisture retrieval from multi-temporal SAR data, the missed alarms are the source of error, but the FAR is also important because it controls the retrieval rate which is defined as the percentage of areas that can be used in soil moisture retrieval. As an example, with all paddocks identified as changed ($AR = 1$; $FAR \sim 1$) no errors will be introduced because the entire image cannot be used in soil moisture retrieval.

In addition, the multi-temporal soil moisture retrieval algorithm proposed by Wagner et al. (1999a) was used to show the effect of s and VWC changes on retrieval before and after the change detection. Specifically, the Wetness Index (WI: 0 to 100%) for a grid is defined as (Wagner et al., 1999a):

$$WI = \frac{\sigma^0 - \sigma^0_{dry}}{\sigma^0_{wet} - \sigma^0_{dry}}, \tag{4}$$

where σ^0, $\sigma_{dry}{}^0$, and $\sigma_{wet}{}^0$ are the current backscatter values at HH polarization of a target grid, and that of the wettest and driest conditions, respectively. Fig. 4(b) shows the concept of the validation process using the WI. The time series σ^0 was first separated into two sub-series at the detected change date k' (parts 7 and 8 in Fig. 4b). Three WIs can be calculated: i) one without removing the effect of roughness and VWC changes (WI_u); ii) one with all changes being removed using the ground truth (WI_{gt}); and iii) one with changes removed by the proposed method (WI_c). The root mean square error (RMSE) of WI_c and WI_u were then calculated taking WI_{gt} as the truth. Accordingly, the RMSE of WI_c and WI_u can be treated as the initial and residual error caused by the s and VWC changes before and after change detection, respectively.

4. Methodology

The proposed change detection method consists of two components (Fig. 5): (i) feature selection and extraction at the paddock scale, and (ii) determination of the change maps. The first component intends to extract the optimal features of paddocks for effectively detecting the anomaly surface changes. The second component is a two-step procedure to identify the changed paddocks, where multiple over-detected change maps for the period of interest are first generated using a simple

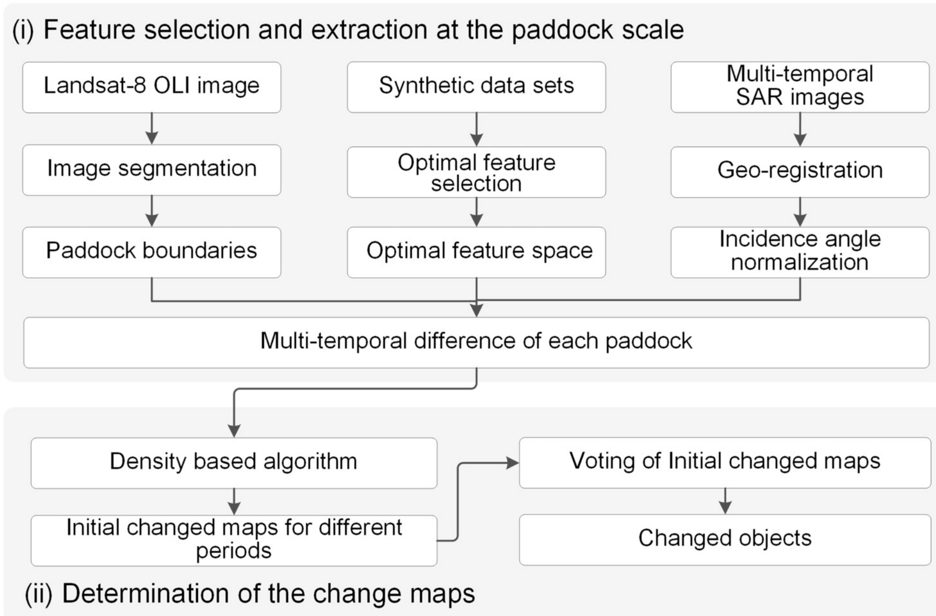

Fig. 5. Flowchart of the proposed change detection method.

density-based method and then merged using a "voting" to remove the false changed paddocks.

4.1. Feature selection and extraction at the paddock scale

As previously addressed, anomaly surface change detection is more suitable to be carried out at the paddock scale within the optimal feature space. Accordingly, a Landsat 8 OLI image was used to provide the paddock boundaries. Several difference/ratio images were then extracted using pixel-wise algebraic operations to provide candidates for an optimal feature space, which were then further determined using a genetic algorithm (GA) based feature selection. Following the extracted boundaries and corresponding difference/ratio values calculation, the mean vector of each paddock was calculated over the optimal space. These vectors were then normalized to be between 0 and 1 along each dimension as the input to the change detection algorithm. The process is detailed as follows:

A. **Paddock extraction**. The boundaries of paddocks are extracted using a range of image segmentation algorithm; several available algorithms were comprehensively evaluated in Zhang et al. (2015). In this study, the multi-resolution segmentation algorithm (Baatz, 2000) embedded in the commercial software eCognition Developer 8 was used, with the scale and shape parameters being 10 and 0.5, respectively, considering the size and shape of paddocks in the study area.
B. **Calculation of backscatter difference/ratio images**. The candidate difference/ratio images are listed in Table 3. The difference and ratio images of two temporally adjacent acquisitions t and $t-1$ in dB can be calculated as:

$$f^1(x, y) = f_{pq}^{t}(x, y) - f_{pq}^{t-1}(x, y), \tag{5}$$

$$f^2(x, y) = f_{pq}^{t}(x, y)/f_{pq}^{t-1}(x, y), \tag{6}$$

where p and q refer to H and V polarization, and x and y are the row and column of a pixel in the image. The number of possible features for fully polarized data is 18, resulting in a large number of available feature combinations ($2^{18} = 262{,}144$) for subsequent refinement using the feature selection algorithm below.

C. **Optimal feature space selection**. A range of feature selection algorithms are available (see Guyon and Elisseeff (2003) for an introduction and review). Among these, genetic algorithms (GA) are a well-known general adaptive optimization method that can efficiently process large search spaces with a low risk of reaching a local optimum (Guyon and Elisseeff, 2003). Hence, a GA was employed as the search algorithm in this study to find the optimal feature space.

A GA is a metaheuristic searching algorithm inspired by the process of natural selection. The first step of a GA is chromosome design and population initialization. For fully polarized data, the chromosome is an 18-bit binary value, corresponding to the 18 available features listed in Table 3. In the population initialization, 20 chromosomes were randomly generated with several bits of each chromosome being 1, denoting the initial selected features. These chromosomes were then adaptively optimized using three genetic operations, i.e. selection, crossover, and mutation. The selection operation was used to pick good chromosomes from the current population according to the fitness function defined in this study as:

$$fitness = \sqrt{2(1 - e^{-\alpha})} \cdot e^{-Ns/Na}, \tag{7}$$

Table 3
Candidature feature index for SAR data acquired at time t and $t-1$.

Family (#)	Candidature features
Difference (6)	$HH_t - HH_{t+1}$, $HH_t - HV_{t+1}$, $HH_t - VV_{t+1}$, $HV_t - HV_{t+1}$, $HV_t - VV_{t+1}$, $VV_t - VV_{t+1}$
Ratio (6)	HH_t/HH_{t+1}, HH_t/HV_{t+1}, HH_t/VV_{t+1}, HV_t/HV_{t+1}, HV_t/VV_{t+1}, VV_t/VV_{t+1}
Second order features (6)	$HV_t/VV_t - HV_{t+1}/VV_{t+1}$, $HV_t/HH_t\text{-}HV_{t+1}/HH_{t+1}$, $HH_t/VV_t - HH_{t+1}/VV_{t+1}$, $(HV_t/VV_t)/(HV_{t+1}/VV_{t+1})$, $(HV_t/HH_t)/(HV_{t+1}/HH_{t+1})$, $(HH_t/VV_t)/(HH_{t+1}/VV_{t+1})$

$$\alpha = \frac{1}{8}(\mu_i - \mu_j)^T\left(\frac{C_i + C_j}{2}\right)^{-1}(\mu_i - \mu_j) + \frac{1}{2}\ln\left(\frac{1}{2}\ |C_i + C_j|/\sqrt{|C_i||C_j|}\right), \tag{8}$$

where μ_i and μ_j are the mean vector of class i and j (change or unchanged), respectively; C_i and C_j are the covariance matrix of class i and j, respectively; Ns and Na denote the number of selected features and number of all available features, respectively. The first term of the fitness function, i.e. $\sqrt{2(1 - e^{-\alpha})}$, is known as the Jeffreys-Matusita (J-M) distance ($0 - \sqrt{2}$) which is a commonly used metric of interclass separability (Bruzzone et al., 1995). Two classes are partly to fully separable if the J-M distance is larger than 1. The rest of the fitness function is used to limit the number of selected features considering the computational efficiency in the change detection.

The crossover operator refers to the exchange of several bits between two chromosomes, and the mutation operator is used to improve the genetic diversity by randomly modifying some part of a chromosome. Both crossover and exchange can help avoid local optima by exploring new regions of search space. The optimization process is terminated when the number of iterations (also known as generations) reaches a defined value. In this study, the maximum generation, population size, crossover rate, and mutation rate were 100, 20, 0.1, and 0.01 respectively.

4.2. Determination of the change maps

After the previous step, each paddock corresponds to a feature vector in the selected optimal feature space and a set of thresholds or a hyper-plane is required to separate the changed paddocks from those that are unchanged. A number of methods can be used to achieve an accurate hyper-plane with some assumptions and/or iterative optimization (Bazi et al., 2005; Gong et al., 2012). Despite the satisfactory performance in specific applications, the main drawback of these methods is the complexity to be a pre-processing stage of multi-temporal soil moisture retrieval. A simple strategy inspired by the ensemble machine learning is used here. In the framework of ensemble leaning (Zhang and Ma, 2012), the combination of multiple poor to moderate results from different leaners is expected to result in an accurate result. Similarly, the combination of multiple over-detected change maps for the period of interest derived from different SAR pairs are also expected to have a satisfactory result. Generating over-detected change maps is easier than an accurate one.

Given a time series of SAR images $O = \{O_1, \ldots, O_k, \ldots, O_t\}$, the anomaly surface changes that occurred between the acquisitions $t - 1$ and t are recorded by $t - 1$ SAR pairs $O_t/O_{t-1}, \ldots, O_t/O_k, \ldots, O_t/O_1$ ($1 < k < t - 1$). Based on these SAR pairs, $t - 1$ over detected change maps $C = \{C_{t,t-1}, \ldots, C_{t,k} \ldots, C_{t,1}\}$ ($1 < k < t - 1$) can be generated. Obviously, a change map $C_{t,k}$ includes not only the changed paddocks for the target period ($t - 1$ and t) but also these for the period of $t - 1$ to k. The latter can be removed by simply subtracting the change map $C_{t-1,k}$ generated from O_{t-1}/O_k from the $C_{t,k}$. Accordingly, $t - 1$ change maps for the target period are generated $C = \{C_{t,t-1}, \ldots, C_{t,k} - C_{t-1,k}, \ldots, C_{t,1} - C_{t-1,1}\}$ ($1 < k < t - 1$). These poor to moderate change maps were finally merged to get a more accurate one through:

$$C = \sum_k (C_{t,k} - C_{t-1,k}) \geq N_k - 1, (1 < k < t), \tag{9}$$

where N_k is the number of k. A straightforward explanation of Eq. (9) is as follows: multiple change maps for the period t and $t - 1$ can be treated as independent "voters" which are more likely to vote the real changed paddocks. The maximum number of votes that one paddock can get is N_k, with the real changed paddocks expected to receive near N_k votes, which is significantly larger than that of falsely identified paddocks. Accordingly, a threshold $N_k - 1$ can help remove most of the false alarms. An example of how multiple change detection results are merged is provided in Fig. 6 using the time series L-band data.

Eq. (5) requires multiple over-detected change maps which are generated using a simple clustering algorithm, i.e. Density-Based Spatial Clustering of Applications with Noise (DBSCAN) (Ester et al., 1996). DBSCAN is capable of dealing with a large dataset and discovering clusters with arbitrary shape and noise without predetermination of a cluster number. Since the DBSCAN is only used to identify the noise which is the changed paddocks in this study, only a brief introduction relating to the noise is included; please refer to Ester et al. (1996) for detail.

In DBSCAN (Ester et al., 1996), a point p_i of a dataset $\boldsymbol{P}$ belongs to one of the following three types: core point, border point, and noise. The definitions of these types are based on the conception of local density D (p_i) = Cardinality (N_{Eps} (p_i)), where N_{Eps} (p_i) is the number of neighbour points of p_i within a given radius (Eps) defined as $N_{Eps}(p_i) = \{p_j | \forall j, \text{distance}(p_i, p_j) < Eps\}$. In other words, this refers to the number of points within a radius Eps. A core point p_c refers to a point containing at least a user-defined minimum number of other points ($MinPts$) within Eps, i.e. D (p_c) ≥ $MinPts$. A noise point p_n refers to one that does not contain core points in their neighbours and D (p_n) < $MinPts$.

The selection of Eps and $MinPts$ is key to the success of DBSCAN (Khan et al., 2014). For cases with prior-knowledge of the percentage of noise, the Eps can be determined using the $MinPts$-dist graph (Ester et al., 1996). In this study, the DBSCAN was not used to generate accurate change maps, but one that includes all potential changed paddocks. A relatively large percentage of noise (15%) was set for over-detecting paddocks, which will be refined in the ensemble detection.

5. Results

5.1. Experiment design

Three experiments were designed to evaluate the performance of the proposed method. The parameter N_k was set to 3, indicating that four SAR images in the time series were used to produce three over-detected change maps in the single detection step, with these merged in the ensemble detection. The determination of such a value is due to the availably of multi-temporal images in a short time span for a reduced effect of gradual roughness and vegetation changes (e.g., 24 days for 4 Sentinel-1 A/B observations). The detail of each experiment is introduced below with the input data sets described in Table 4.

A. The first experiment was designed to select the optimal feature spaces for roughness and/or VWC changes based on two synthetic data sets (DS-1 and DS-2). Specifically, optimal feature spaces for L-, C-, and X-band and two polarization modes i.e., Quad (HH + HV + VH + VV) and Dual (VH + VV), were selected. These optimal spaces are therefore independent from the later change detection over the real data set.
B. The proposed change detection method was comprehensively evaluated in the second experiment using the optimal spaces selected in Experiment A. The evaluation was first carried out on DS-1 and DS-2 to show the performance at different frequencies and incidence angles, followed by an investigation on the effect of noise and change amplitude using DS-3.
C. The time series of PLIS, RADARSAT-2 and COSMO SkyMed images (Fig. 2) were used in the last experiment to show the performance on a real data set.

All synthetic data were generated ten times with different random presence/absence of roughness and VWC changes and thus ten values are available for each validation metric. The mean and standard deviation of these values was reported below to show the average performance and stability of the proposed method. For simplicity, F score, AR, and FAR are used to denote the average F score, AR, and FAR of the 10 trials hereafter.

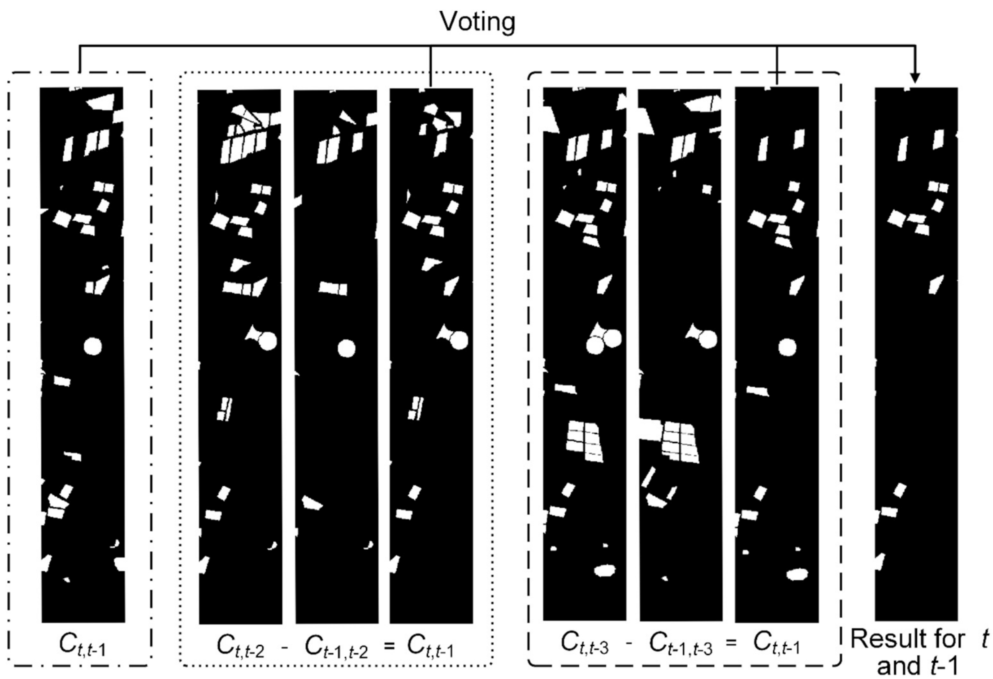

Fig. 6. An example showing the process of generating the change map for the period of t and $t-1$ using an L-band series. White paddocks are those identified as changed. The label C refers to over-detected maps with the subscripts denoting the periods. Three over-detected maps for the periods of t and $t-1$ were generated first and then merged to remove the false alarms.

Table 4
Synthetic data sets used in this study. DS denotes dataset.

	Frequency (GHz)	Incidence angle (°)	Look #	Types of anomaly changes
DS1	1.26 & 5.41	20, 30, 40, 50	1	VWC & roughness
DS2	9.3	20, 30, 40, 50	1	Roughness
DS3	1.26	30	1:2:11	VWC & roughness

5.2. Optimal feature space

Table 5 introduces the optimal feature space identified for different radar configurations (frequency and polarization). In general, the J-M distance for all cases was larger than 1.28 showing a satisfactory separability between changed and unchanged paddocks in the selected feature space. The number of selected features was relatively small (3–4) compared to the 18 available features for fully polarized data. More specifically, the $HV_t/VV_t - HV_{t+1}/VV_{t+1}$ combination was selected by all radar configurations, followed by the $VV_t - VV_{t+1}$, $HV_t - HV_{t+1}$, and HV_t/HV_{t+1}, which were selected in 5, 3 and 2 cases, respectively. Since $VV_t - VV_{t+1}$, and VV_t/VV_{t+1} are highly correlated, the features based only on time series VV were selected by all configurations. Similarly, time series of HV polarization were selected in 5 cases, including either $HV_t - HV_{t+1}$ or HV_t/HV_{t+1}. These results can be explained by the different sensitivities of features to surface changes. For example, the cross-polarized ratio (HV/VV) is very sensitive to the change of roughness, especially for roughness changes at small values ($ks < 2$ where k is the wavenumber; Oh, 2004), while the HV polarization is sensitive to both VWC and roughness changes (Ulaby et al., 2014). The VV polarization has larger attenuation than HH over vegetation with a dominant vertical structure (e.g., wheat) and thus VWC changes can result in larger changes in VV. Despite the great similarity, slight changes in feature constitution were observed among different radar configurations, which may result from the existence of multiple solutions with similar fitness values.

L-band achieved the largest J-M distance in both Quad and Dual polarized data, followed by C- and X-band. However, the difference was limited with the largest difference (0.16) observed between L-band Quad and X-band Dual. Quad data achieved a slightly larger J-M distance than Dual data for L- and X-band, with the aid of an additional

Table 5
Selected (those with a ×) optimal feature space and the corresponding J-M distance for different radar configurations based on synthetic SAR data sets with various surface changes, where the grey grids denote the unavailable features. Q and D denote Quad and Dual (HV + VV) polarization, respectively.

Feature	X-band		C-band		L-band	
	Q	D	Q	D	Q	D
$HH_t - HH_{t+1}$						
$HH_t - HV_{t+1}$						
$HH_t - VV_{t+1}$						
$HV_t - HV_{t+1}$	×		×	×		
$HV_t - VV_{t+1}$		×				
$VV_t - VV_{t+1}$		×	×	×	×	×
HH_t/HH_{t+1}						
HH_t/HV_{t+1}						
HH_t/VV_{t+1}	×					
HV_t/HV_{t+1}					×	×
HV_t/VV_{t+1}						
VV_t/VV_{t+1}	×					
$HV_t/VV_t - HV_{t+1}/VV_{t+1}$	×	×	×	×	×	×
$(HV_t/VV_t)/(HV_{t+1}/VV_{t+1})$						
$HV_t/HH_t - HV_{t+1}/HH_{t+1}$						
$(HV_t/HH_t)/(HV_{t+1}/HH_{t+1})$						
$H_t/VV_t - HH_{t+1}/VV_{t+1}$						
$(HH_t/VV_t)/(HH_{t+1}/VV_{t+1})$					×	
J-M distance	1.32	1.28	1.35	1.35	1.39	1.37

feature related to the co-polarized ratio (HH/VV); i.e. HH_t/VV_{t+1} for X-band and $(HH_t/VV_t)/(HH_{t+1}/VV_{t+1})$ for L-band. The effect of HH/VV here is unclear, because i) the elevation angle of vegetation was assumed to follow a fixed distribution and thus VWC changes cannot introduce significant changes in HH/VV; and ii) HH/VV is relatively insensitive to roughness changes, changing from 0.6 dB to 3.5 dB when σ changes from 0.3 to 4.8 cm at C-band (Oh, 2004). Accordingly, a uniform feature space including the $HV_t/VV_t - HV_{t+1}/VV_{t+1}$, HV_t/HV_{t+1} and $VV_t - VV_{t+1}$ was sufficient for all radar configurations listed in Table 4. The *J*-M distances in this space were around 1.37, 1.34 and 1.27 for L-, C- and X-band, respectively.

This does not mean however that dual polarized data are sufficient for all future applications. For example, HH may be required for vegetated areas with more complex structures (e.g., soybean). In addition, the effect of vegetation structure and its interaction with VWC changes were not considered, because of the simplistic vegetation scattering representation in the DBA (Lang and Sighu, 1983). To address this, the Numerical Maxwell Model of three-dimensional simulations (Tsang et al., 2017) can be promising, as this model can fully simulate the scattering of vegetation in detail. The polarimetric parameters calculated from fully polarized data (Cloude and Pottier, 1996) are expected to be more sensitive to the vegetation structure changes than a simple polarization difference/ratio. Finally, the J-M distance is only part of the cost function used in the feature selection, with a more complex feature space potentially providing a better performance for full polarized data at the expense of a drastic increase in computational load.

5.3. Evaluation using synthetic data sets

Fig. 7 shows the performance of the proposed method on single-look synthetic data with different frequencies and incidence angles. In general, moderate performance was achieved in all cases with the *F* score, *AR* and *FAR* ranging from 0.81 to 0.87, 0.76 to 0.82 and 0.09 to 0.15, respectively. The proposed method performed best at L-band, followed by C- and X-bands but only with a slight *F* score difference (< 0.06). These results are coincident with the difference of J-M distance listed in Table 5. The standard deviation of *F* score, *AR* and *FAR* were all < 0.02 showing a good stability of the proposed method. All three metrics demonstrated no clear angular pattern although the same roughness and/or VWC change resulted in quite different backscatter changes at different incidence angles. This can be partly explained by the multiple dependence of detection accuracy on the sensitivity of radar configuration, noise level and spatial variation of moisture changes. For time series with slight roughness and vegetation changes, noise could be the dominant factor resulting in a similar detection accuracy at different incidence angles regardless of the difference in sensitivity. The binary process (absence/presence) in change detection could be another reason. For those paddocks with large roughness and vegetation changes, the backscatter changes at low sensitivity radar configurations (e.g., small incidence angles) could be large enough to be identified.

Despite the moderate performance in view of accuracy metrics (Fig. 7a–c), the proposed method can greatly remove the error caused by roughness and VWC changes in multi-temporal soil moisture retrieval as depicted in Fig. 7(d). About 68.3% (L-band), 74.5% (C-band) and 74.8% (X-band) of the initial RMSE was removed after change detection. The residual RMSE was < 8%, 7% and 3% for L-, C-, and X-band respectively. This difference is mainly caused by the different

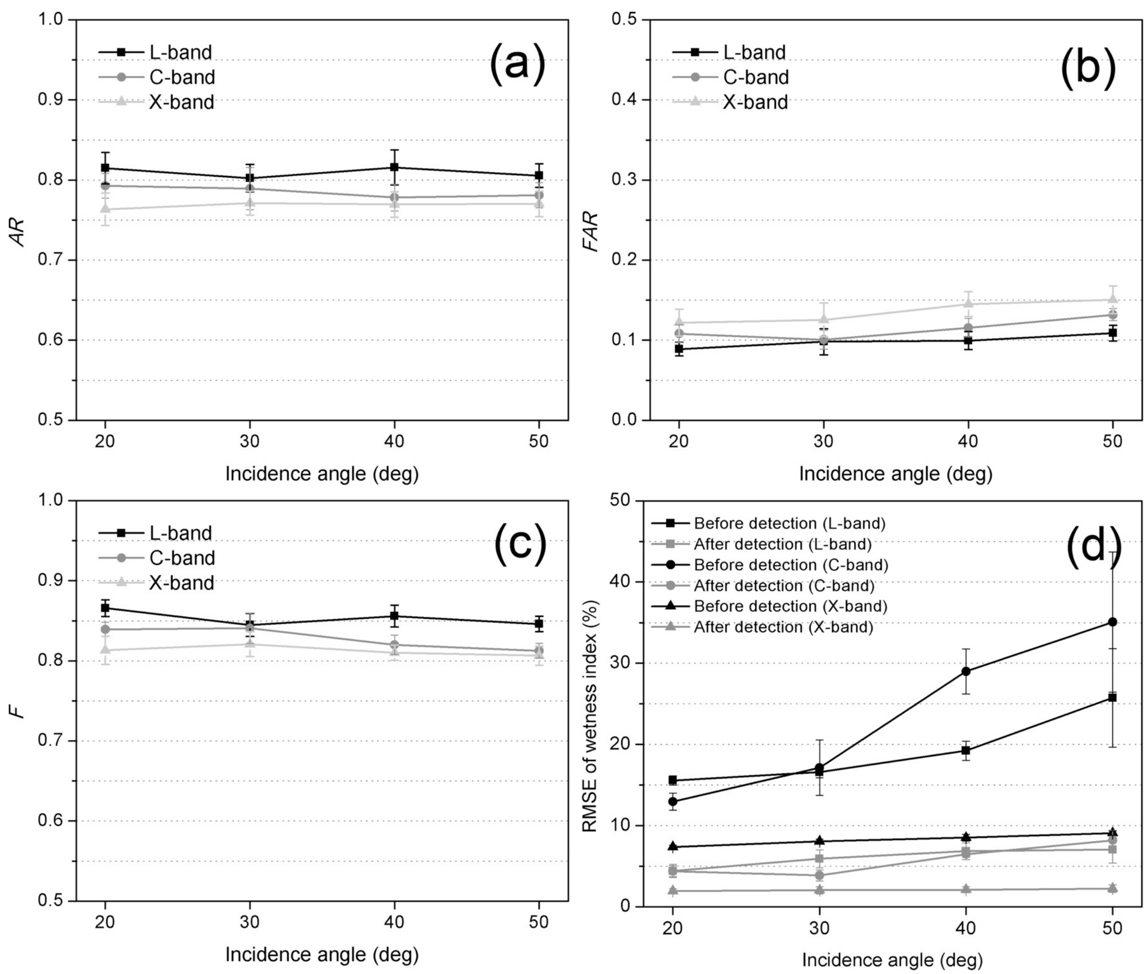

Fig. 7. Performance of the proposed method on single-look synthetic data sets. (a)–(d) are the *AR*, *FAR*, *F* and RMSE of wetness index at L-, C- and X-bands with various incidence angles, respectively. The error bars denote the standard deviation of metrics.

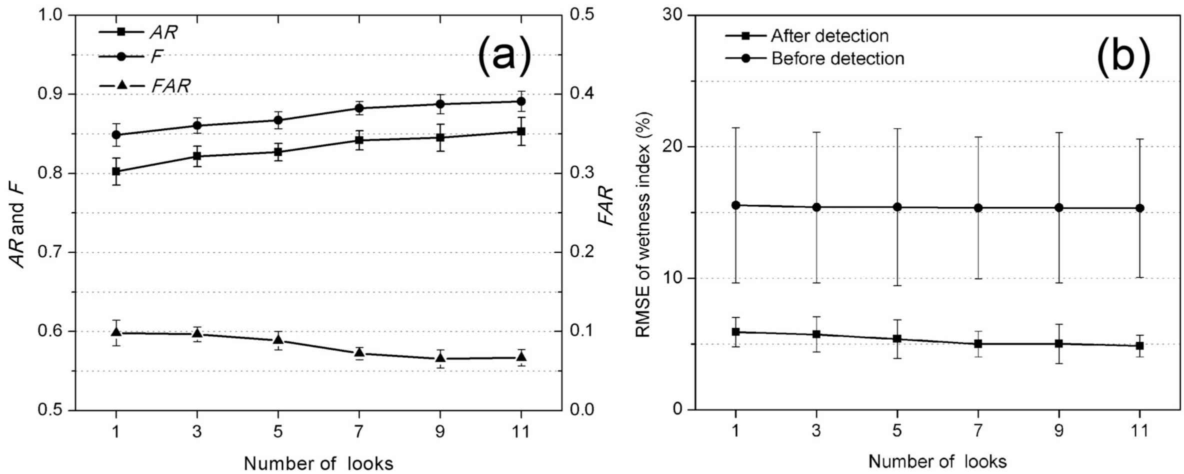

Fig. 8. Impact of noise on performance using L-band synthetic data. Panel (a) shows the average *AR*, *FAR*, and *F* versus the number of looks; panel (b) shows the RMSE of wetness index versus the number of looks. The error bars denote the standard deviation of metrics.

amount of changed paddocks. At X-band, 10% of bare soil paddocks had random roughness changes, while additional VWC changes in 10% of the vegetated paddocks were included at L- and C-bands. Significant angular dependence of RMSE was observed at L- and C-bands. This is mainly caused by the heavy dependence of backscattering coefficient on incidence angle and frequency over vegetated areas. The same VWC change at larger incidence angles and/or higher frequencies resulted in larger backscattering coefficient changes and consequently larger error in the multi-temporal retrieval. In contrast, the same roughness change at different angles resulted in similar backscattering coefficient changes and thus no clear angular pattern being observed in the results of X-band. For instance, a *s* change from 0.3 cm to 3 cm results in a HH difference of 8.1 dB at an incidence angle of 20° according to the Oh model, which is 10.0 dB at 50° given a soil moisture value of 0.3 m^3/m^3.

The relationship between the performance and the number of independent looks for L-band is presented in Fig. 8, where a larger number of looks indicates a lower noise level. As expected, *AR* and *F* gradually increased as noise decreased and reached their highest values when the number of looks was larger than 7, while the opposite was found for *FAR*. This is consistent with the process of noise reduction using the multi-look operation. The main part of the noise was removed changing the number of looks from 1 to 7, with further multi-looking contributing little to the result. After removing the major part of the noise, a satisfactory performance was achieved with an *F* score, *AR* and *FAR* of 0.90, 0.85, and 0.07, respectively. However, the improvement in the residual RMSE of wetness index was negligible (~1%), as depicted in Fig. 8(b). One explanation is that the improvement in *AR* mainly comes from additional identification instances of small roughness and VWC changes whose effect on radar observations is close to the noise level. Such small roughness and VWC changes could only have a limited effect on multi-temporal soil moisture retrieval, thus with negligible improvement.

A further investigation on the relationship between detection accuracy and surface change amplitude in percentage for single-look L-band data is presented in Fig. 9. The proposed pre-processing method had a relatively poor performance in identifying small roughness and VWC changes with an *AR* of 0.62 for a 10% change, but fortunately the effect of these small changes on multi-temporal soil moisture retrieval is also small. The residual RMSE in wetness index after change detection is only 2.46%. An important implication based on this is that the gradual (natural) roughness and VWC changes should not have a significant effect on soil moisture retrieval. When the amplitude of roughness and VWC change increased from 10% to 70%, *AR* and *F* increased from 0.62 to 0.90 and 0.68 to 0.92 respectively, with a sharp *FAR* decrease of 0.19. However, the residual RMSE in soil wetness first slightly increased from 2.46% to 7.32% and then decreased to 4.01%. This can be explained by the different effects of surface change amplitude on *AR* and RMSE. The RMSE of the wetness index relates to the number of missed alarms and the absolute error caused by a single missed alarm. Paddocks with larger change amplitudes are easier to be identified, resulting in a reduced number of missed alarms and thus a positive contribution to RMSE. But failure identification of paddocks with larger change amplitudes can introduce larger errors in moisture retrieval than those with smaller amplitudes, being a negative effect on RMSE. For change amplitudes < 40%, the negative effect is larger than the positive, which was reversed for larger surface changes.

5.4. Evaluation using real observational data set

The sudden surface change detection results over time series of PLIS, RADARSAT-2 and COSMO SkyMed acquisitions are presented in Fig. 10, with the dashed lines showing the start and end time of the period of interest for each change map. The detection agreement is shown in light grey for the unchanged paddocks and in blue for the changed paddocks. The false alarms and missed alarms are depicted in dark grey and green, respectively. In general, the proposed method achieved satisfactory results for L- and C-band data. Only one changed paddock was missed for the L-band data with a total of 9 false alarms. Despite the relatively high *FAR* (0.3), only one paddock was erroneously identified as changed twice in this period (the red circle in Fig. 10). These false alarms only have a negative influence on soil moisture retrieval methods that need a long time series of SAR data (e.g., Wagner et al., 1999a). Taking the paddock in the red circle in Fig. 10 as an example, it was falsely detected as changed between DOY 260–262 and DOY 265–267. Consequently, the relevant time series of the L-band observations should be separated into three sub-series, i.e. DOY 255–260, DOY 262–265, and DOY 267-end. Soil moisture retrieval algorithms can subsequently be applied on these respective sub-series.

In the detection results of C-band, acceptable results (*AR* 0.91; *FAR* 0.09) were achieved with two false and two missed alarms. This demonstrates the robustness of the proposed method in dealing with time series images acquired by different observation modes, with the assistance of a simple incidence angle normalization process. However, the detection results for X-band data were much poorer. A number of changed paddocks for DOY 263–269 were not identified. This is mainly caused by the feature space used in X-band; the COSMO SkyMed data only has HH polarization which is not sufficient to detect all changed paddocks.

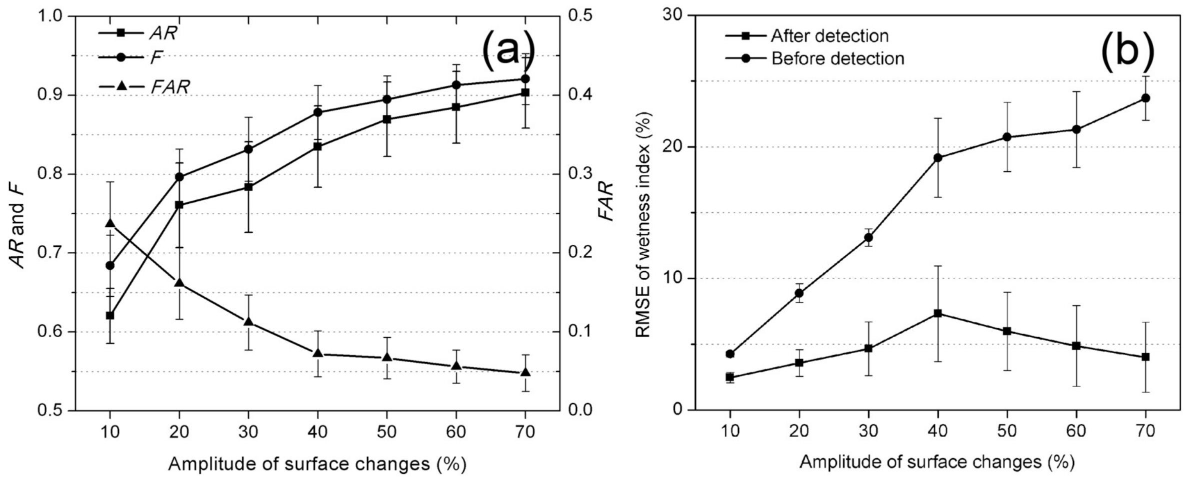

Fig. 9. Impact of roughness and VWC change amplitude on performance using L-band synthetic data. Panel (a) shows the average *AR*, *FAR*, and *F* versus change amplitude; panel (b) shows the RMSE of wetness index versus change amplitude. The error bars denote the standard deviation of metrics.

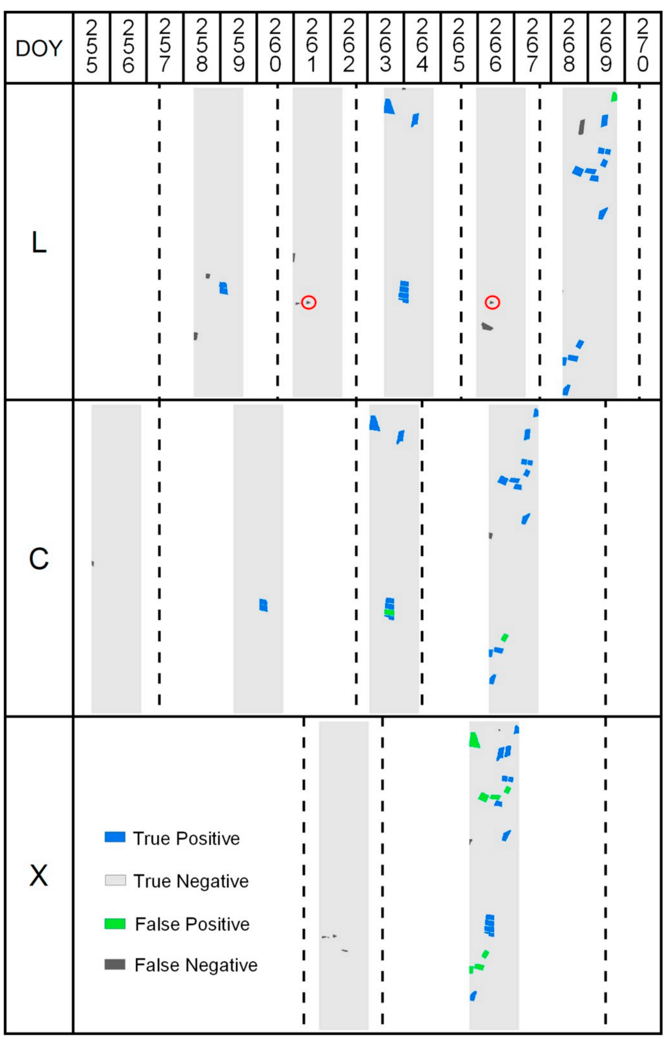

Fig. 10. Change detection results versus ground truth using real SAR data collected during the SMAPEx-5 study period. The dashed lines show the start and end time of the period of interest for each change map.

6. Discussion

The objective of the proposed pre-processing method is to identify abrupt roughness and vegetation changes caused by cultivation activities, to ensure that the soil moisture variation is the only source of backscattering variation for the time period being processed for soil moisture. However, a few other factors may also result in backscattering variation in time (Fig. 11). Variation of the SAR system can also introduce significant changes in SAR observations (Ulaby et al., 2014), creating a problem in the change detection-type methods (Wagner et al., 1999a), while also providing a great opportunity for methods using the characteristic of multi-configuration, e.g., van der Velde et al. (2012). Relative geometric and calibration errors are tightly related to a specific SAR system so data acquired from the same observation geometry commonly has great stability, while combining images with different acquisition modes and/or incidence angles may introduce large uncertainties. A simple strategy to avoid these changes is to identify the changes using the same source of SAR data first and then merge the backscatter change maps from different SAR sources using simple map algebraic operation. For soil moisture retrieval from time series multi-SAR data, a robust scattering model is required to represent the different scattering behaviors in various radar configurations.

The proposed method only achieved a moderate detection accuracy with the *AR* and *FAR* ranging from 0.75 to 0.85 and 0.08 to 0.15 for single-look data. These are lower than the results of other methods in identifying the change of landcover types (Marin et al., 2015; Pantze et al., 2014), flooded area (Brisco et al., 2013), ship (Wei et al., 2014) and oil spills (Konik and Bradtke, 2016), which commonly have an *AR* and *FAR* of better than 0.9 and 0.1 respectively. However, detecting soil roughness and VWC changes is more challenging, as the amplitudes of these changes are much smaller than that of landcover type change, presence/absence of a ship etc. Despite the relatively low accuracy, satisfactory results were achieved in view of the residual error in soil moisture retrieval. Notably, the method was only evaluated based on the SMAPEx-5 scenario (a smooth dry down period), with sudden moisture changes due to irrigation and rainfall treated as anomaly changes. In addition, the proposed method can work in an unsupervised and fast way without any prior assumptions about the data distribution. DBSCAN which was originally applied to discover cluster structures (Ester et al., 1996) was used here to over-detect noise (changed paddocks) by simply setting an overestimated noise percentage.

To serve as a pre-processing procedure of operational global soil moisture retrieval, the proposed method should be further simplified, with the step of paddock extraction using image segmentation being

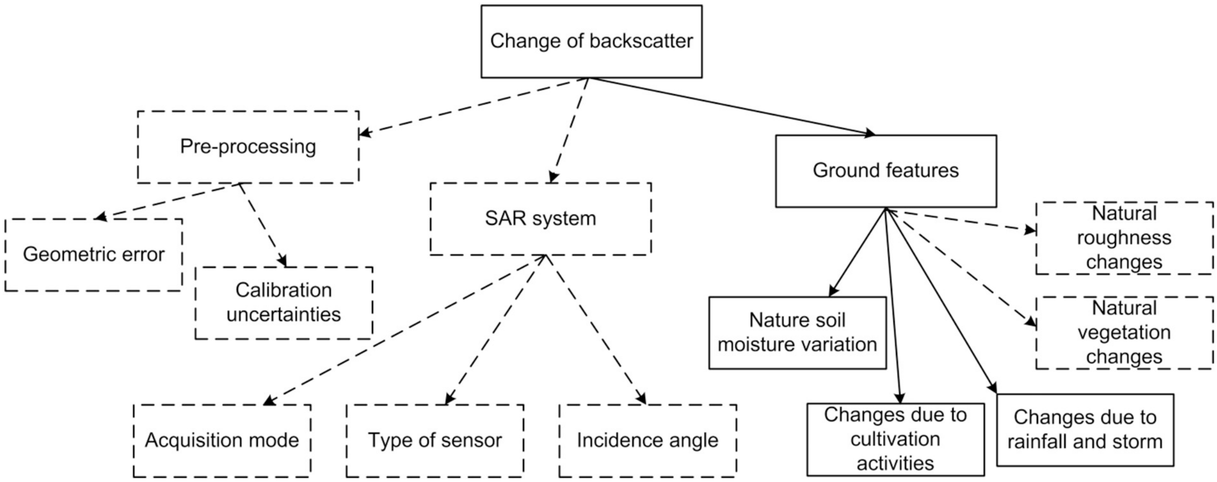

Fig. 11. Flowchart showing the factors affecting backscatter changes from multi-temporal SAR images. The solid rectangles at the bottom level show the sources being considered in this study.

inconvenient for real-time applications. But this step can be carried out independently and it is unnecessary to extract the paddocks every time before detecting the changed paddocks. Alternatively, land use data or patches of a landcover map can be roughly treated as paddocks in global application. Several global land cover maps (e.g., Chen et al., 2015; Gong et al., 2013) with a spatial resolution of 30 m are available for this. The selection of optimal feature space can also be carried out independently based on more observations of surface cultivation. Otherwise, the feature spaces selected in this study can be used directly because the selection of these feature spaces is independent of the specific study area. Finally, the DBSCAN can be directly replaced by its parallel version (Xu et al., 2002) to deal with the huge global data set.

7. Conclusion

This study introduced an unsupervised method to detect anomaly surface changes, serving as a pre-procedure of soil moisture retrieval from time series SAR images. Briefly, time series data are separated into multiple subseries according to the change detection results. For multi-temporal soil moisture retrieval methods without a calibration process, e.g., Balenzano et al. (2011), Kim et al. (2012), Ouellette et al. (2017) and Zhu et al. (2018a), soil moisture retrieval can be carried out on each sub-series independently. However, for those requiring a calibration or multi-temporal vegetation correction, e.g., the Wagner et al. (1999a) and Pierdicca et al. (2010), the proposed method could provide an alarm for potential uncertainty caused by roughness and vegetation changes. This method includes two main steps; i) generating multiple over-detected surface change maps in the selected optimal feature space, i.e. the space spanned by the temporal ratio of VH and the temporal difference of VV and VH/VV, and ii) combining multiple change maps to get a robust change map. Evaluation on synthetic data sets demonstrated that the proposed approach can effectively eliminate the major part of error in multi-temporal soil moisture caused by roughness and VWC changes, although only a moderate *AR* (0.75–0.85) and *FAR* (0.08–0.15) was achieved for single look data. Experiments on real L- and C-band data also confirmed the effectiveness of the method showing an accurate identification of changed paddocks (> 0.9) and a low false-alarm rate (< 0.1).

Acknowledgements

The SMAPEx-5 field campaigns were supported by an Australian Research Council Discovery Project (DP140100572). Thanks to the Italian Space Agency (ASI) for providing the COSMO-SkyMed products, and MacDonald, Dettwiler and Associates Ltd. for making RADARSAT-2 products available (RADARSAT-2 Data and Products ©MacDonald, Dettwiler and Associates Ltd. (2015) — All rights reserved). The authors also acknowledge the scholarships awarded by China Scholarship Council (CSC), Australian Research Council (ARC) and Monash University to support Liujun Zhu's PhD research.

References

Baatz, M., 2000. Multiresolution segmentation: an optimization approach for high quality multi-scale image segmentation. Angew. Geogr. Inform. 12–23.
Baghdadi, N., King, C., Chanzy, A., Wigneron, J., 2002. An empirical calibration of the integral equation model based on SAR data, soil moisture and surface roughness measurement over bare soils. Int. J. Remote Sens. 23, 4325–4340.
Baghdadi, N., Gherboudj, I., Zribi, M., Sahebi, M., King, C., Bonn, F., 2004. Semi-empirical calibration of the IEM backscattering model using radar images and moisture and roughness field measurements. Int. J. Remote Sens. 25, 3593–3623.
Balenzano, A., Mattia, F., Satalino, G., Davidson, M.W., 2011. Dense temporal series of C- and L-band SAR data for soil moisture retrieval over agricultural crops. IEEE J. Select. Top. Appl. Earth Observations Remote Sens. 4, 439–450.
Balenzano, A., Satalino, G., Lovergine, F., Rinaldi, M., Iacobellis, V., Mastronardi, N., Mattia, F., 2013. On the use of temporal series of L-and X-band SAR data for soil moisture retrieval. Capitanata plain case study. Eur. J. Remote Sensing 46, 721–737.
Bazi, Y., Bruzzone, L., Melgani, F., 2005. An unsupervised approach based on the generalized Gaussian model to automatic change detection in multitemporal SAR images. IEEE Trans. Geosci. Remote Sens. 43, 874–887.
Blaes, X., Defourny, P., 2008. Characterizing bidimensional roughness of agricultural soil surfaces for SAR modeling. IEEE Trans. Geosci. Remote Sens. 46, 4050–4061.
Bolter, R., Gelautz, M., Leberl, F., 1996. SAR speckle simulation. Int. Arch. Photogramm. Remote Sens. 31, 20–25.
Brisco, B., Schmitt, A., Murnaghan, K., Kaya, S., Roth, A., 2013. SAR polarimetric change detection for flooded vegetation. Int. J. Digital Earth 6, 103–114.
Bruzzone, L., Prieto, D.F., 2002. An adaptive semiparametric and context-based approach to unsupervised change detection in multitemporal remote-sensing images. IEEE Trans. Image Process. 11, 452–466.
Bruzzone, L., Roli, F., Serpico, S.B., 1995. An extension of the Jeffreys-Matusita distance to multiclass cases for feature selection. IEEE Trans. Geosci. Remote Sens. 33, 1318–1321.
Chen, J., Chen, J., Liao, A., Cao, X., Chen, L., Chen, X., He, C., Han, G., Peng, S., Lu, M., 2015. Global land cover mapping at 30 m resolution: a POK-based operational approach. ISPRS J. Photogramm. Remote Sens. 103, 7–27.
Cloude, S.R., Pottier, E., 1996. A review of target decomposition theorems in radar polarimetry. IEEE Trans. Geosci. Remote Sens. 34, 498–518.
van der Velde, R., Su, Z., van Oevelen, P., Wen, J., Ma, Y., Salama, M.S., 2012. Soil moisture mapping over the central part of the Tibetan Plateau using a series of ASAR WS images. Remote Sens. Environ. 120, 175–187.
Ester, M., Kriegel, H.-P., Sander, J., Xu, X., 1996. A density-based algorithm for discovering clusters in large spatial databases with noise. In: Proceedings of Second International Conference on Knowledge Discovery and Data Mining, pp. 226–231 (Portland).
Gong, M., Zhou, Z., Ma, J., 2012. Change detection in synthetic aperture radar images based on image fusion and fuzzy clustering. IEEE Trans. Image Process. 21, 2141–2151.
Gong, P., Wang, J., Yu, L., Zhao, Y., Zhao, Y., Liang, L., Niu, Z., Huang, X., Fu, H., Liu, S., 2013. Finer resolution observation and monitoring of global land cover: first mapping results with Landsat TM and ETM+ data. Int. J. Remote Sens. 34, 2607–2654.
Guyon, I., Elisseeff, A., 2003. An introduction to variable and feature selection. J. Mach.

Learn. Res. 3, 1157–1182.
Huang, S., Tsang, L., 2012. Electromagnetic scattering of randomly rough soil surfaces based on numerical solutions of Maxwell equations in three-dimensional simulations using a hybrid UV/PBTG/SMCG method. IEEE Trans. Geosci. Remote Sens. 50, 4025–4035.
Hunsaker, D., Clemmens, A., Fangmeier, D., 1999. Cultural and irrigation management effects on infiltration, soil roughness, and advance in furrowed level basins. Trans. ASAE 42, 1753–1762.
Hussain, M., Chen, D., Cheng, A., Wei, H., Stanley, D., 2013. Change detection from remotely sensed images: from pixel-based to object-based approaches. ISPRS J. Photogramm. Remote Sens. 80, 91–106.
Khan, K., Rehman, S.U., Aziz, K., Fong, S., Sarasvady, S., 2014. DBSCAN: past, present and future. In: International Conference on the Applications of Digital Information and Web Technologies (ICADIWT). IEEE, Bangalore, India, pp. 232–238.
Kim, S.-B., Tsang, L., Johnson, J.T., Huang, S., Van Zyl, J.J., Njoku, E.G., 2012. Soil moisture retrieval using time-series radar observations over bare surfaces. IEEE Trans. Geosci. Remote Sens. 50, 1853–1863.
Konik, M., Bradtke, K., 2016. Object-oriented approach to oil spill detection using ENVISAT ASAR images. ISPRS J. Photogramm. Remote Sens. 118, 37–52.
Kornelsen, K.C., Coulibaly, P., 2013. Advances in soil moisture retrieval from synthetic aperture radar and hydrological applications. J. Hydrol. 476, 460–489.
Kweon, S.-K., Oh, Y., 2014. Estimation of soil moisture and surface roughness from single-polarized radar data for bare soil surface and comparison with dual- and quad-polarization cases. IEEE Trans. Geosci. Remote Sens. 52, 4056–4064.
Lang, R.H., Sighu, J.S., 1983. Electromagnetic backscattering from a layer of vegetation: a discrete approach. IEEE Trans. Geosci. Remote Sens. 62–71.
Marin, C., Bovolo, F., Bruzzone, L., 2015. Building change detection in multitemporal very high resolution SAR images. IEEE Trans. Geosci. Remote Sens. 53, 2664–2682.
Mattia, F., Satalino, G., Pauwels, V., Loew, A., 2009. Soil moisture retrieval through a merging of multi-temporal L-band SAR data and hydrologic modelling. Hydrol. Earth Syst. Sci. 13, 343–356.
McDonald, K.C., Zimmermann, R., Kimball, J.S., 2002. Diurnal and spatial variation of xylem dielectric constant in Norway spruce (Picea abies [L.] Karst.) as related to microclimate, xylem sap flow, and xylem chemistry. IEEE Trans. Geosci. Remote Sens. 40, 2063–2082.
Notarnicola, C., 2014. A Bayesian change detection approach for retrieval of soil moisture variations under different roughness conditions. IEEE Geosci. Remote Sens. Lett. 11, 414–418.
Oh, Y., 2004. Quantitative retrieval of soil moisture content and surface roughness from multipolarized radar observations of bare soil surfaces. IEEE Trans. Geosci. Remote Sens. 42, 596–601.
Olson, D.L., Delen, D., 2008. Advanced Data Mining Techniques. Springer Science & Business Media.
Ouellette, J.D., Johnson, J.T., Balenzano, A., Mattia, F., Satalino, G., Kim, S.-B., Dunbar, R.S., Colliander, A., Cosh, M.H., Caldwell, T.G., 2017. A time-series approach to estimating soil moisture from vegetated surfaces using L-band radar backscatter. IEEE Trans. Geosci. Remote Sens. 55 (6), 3186–3193.
Pantze, A., Santoro, M., Fransson, J.E., 2014. Change detection of boreal forest using bi-temporal ALOS PALSAR backscatter data. Remote Sens. Environ. 155, 120–128.
Pierdicca, N., Pulvirenti, L., Bignami, C., 2010. Soil moisture estimation over vegetated terrains using multitemporal remote sensing data. Remote Sens. Environ. 114, 440–448.
Rahman, M., Moran, M., Thoma, D., Bryant, R., Collins, C.H., Jackson, T., Orr, B., Tischler, M., 2008. Mapping surface roughness and soil moisture using multi-angle radar imagery without ancillary data. Remote Sens. Environ. 112, 391–402.
Sahebi, M., Angles, J., 2010. An inversion method based on multi-angular approaches for estimating bare soil surface parameters from RADARSAT-1. Hydrol. Earth Syst. Sci. 14, 2355–2366.
Satalino, G., Balenzano, A., Mattia, F., Davidson, M.W., 2014. C-band SAR data for mapping crops dominated by surface or volume scattering. IEEE Geosci. Remote Sens. Lett. 11, 384–388.
Tsang, L., Liao, T.-H., Tan, S., Huang, H., Qiao, T., 2017. Microwave remote sensing of soil, ocean, snow and vegetation based on 3D Numerical Solutions of Maxwell Equations (NMM3D). In: Geoscience and Remote Sensing Symposium (IGARSS), 2017 IEEE International. IEEE, pp. 1413–1414.
Ulaby, F.T., Moore, R.K., Fung, A.K., 1982. Microwave Remote Sensing Active and Passive—Volume II: Radar Remote Sensing and Surface Scattering and Emission Theory. Artech House, Norwood.
Ulaby, F.T., Long, D.G., Blackwell, W.J., Elachi, C., Fung, A.K., Ruf, C., Sarabandi, K., Zebker, H.A., Van Zyl, J., 2014. Microwave Radar and Radiometric Remote Sensing. The University of Michigan Press, Ann Arbor.
Wagner, W., Lemoine, G., Borgeaud, M., Rott, H., 1999a. A study of vegetation cover effects on ERS scatterometer data. IEEE Trans. Geosci. Remote Sens. 37, 938–948.
Wagner, W., Noll, J., Borgeaud, M., Rott, H., 1999b. Monitoring soil moisture over the Canadian Prairies with the ERS scatterometer. IEEE Trans. Geosci. Remote Sens. 37, 206–216.
Wang, S., Li, X., Han, X., Jin, R., 2011. Estimation of surface soil moisture and roughness from multi-angular ASAR imagery in the Watershed Allied Telemetry Experimental Research (WATER). Hydrol. Earth Syst. Sci. 15, 1415–1426.
Wei, J., Li, P., Yang, J., Zhang, J., Lang, F., 2014. A new automatic ship detection method using L-band polarimetric SAR imagery. IEEE J. Select. Top. Appl. Earth Observations Remote Sensing 7, 1383–1393.
Xu, X., Jäger, J., Kriegel, H.-P., 2002. A fast parallel clustering algorithm for large spatial databases. In: High Performance Data Mining, pp. 263–290.
Ye, N., Walker, J.P., Wu, X., Jeu, R.D., Gao, Y., Jackson, T.J., Jonard, F., Kim, E., Merlin, O., Pauwels, V., Renzullo, L.J., Rüdiger, C., Sabaghy, S.C.S.C., Hebel, V., Yueh, S.H., Zhu, L., 2019. “Towards validation of SMAP: SMAPEX-4 &-5,”. In: In: 2016 IEEE International Geoscience and Remote Sensing Symposium, pp. 3469–3472.
Zhang, C., Ma, Y., 2012. Ensemble Machine Learning: Methods and Applications. Springer.
Zhang, X., Feng, X., Xiao, P., He, G., Zhu, L., 2015. Segmentation quality evaluation using region-based precision and recall measures for remote sensing images. ISPRS J. Photogramm. Remote Sens. 102, 73–84.
Zhu, L., Walker, J.P., Tsang, L., Huang, H., Ye, N., Rüdiger, C., 2018a. Soil moisture retrieval over agricultural fields from time series multi-angular L-band radar data. In: 2018 IEEE International Geoscience and Remote Sensing Symposium, pp. 6139–6142.
Zhu, L., Walker, J.P., Ye, N., Rüdiger, C., Hacker, J., Panciera, R., Tanase, M.A., Wu, X., Gray, D., Stacy, N., Goh, A., Yardley, H., Mead, J., 2018b. The Polarimetric L-band Imaging Synthetic aperture radar (PLIS): description, calibration and cross-validation. IEEE J. Select. Top. Appl. Earth Observ. Remote Sensing 1–13.
Zobeck, T.M., Onstad, C., 1987. Tillage and rainfall effects on random roughness: a review. Soil Tillage Res. 9, 1–20.
Zribi, M., Taconet, O., Ciarletti, V., Vidal-Madjar, D., 2002. Effect of row structures on radar microwave measurements over soil surface. Int. J. Remote Sens. 23, 5211–5224.